

Single-Stage Monocular 3D Object Detection with Virtual Cameras

Andrea Simonelli^{△,*,*}, Samuel Rota Bulò[△], Lorenzo Porzi[△], Elisa Ricci^{*,*}, Peter Kutschieder[△]

[△]Mapillary Research, ^{*}University of Trento, ^{*}Fondazione Bruno Kessler

research@mapillary.com

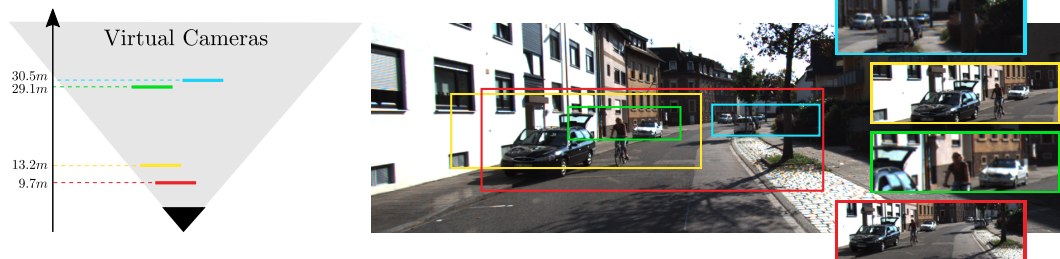


Figure 1: Illustration of the notion of virtual camera. We position virtual cameras in 3D space, ideally nearby potential objects to detect. On the left we see the view windows of some virtual cameras. In the center we see the same views projected on the image plane of the real camera. On the right, we provide the images that we extracted from the virtual cameras, which will be used to train our single-stage 3D object detector. By doing so, we can inject depth invariance in the training process.

Abstract

While expensive LiDAR and stereo camera rigs have enabled the development of successful 3D object detection methods, monocular RGB-only approaches still lag significantly behind. Our work advances the state of the art by introducing MoVi-3D, a novel, single-stage deep architecture for monocular 3D object detection. At its core, MoVi-3D leverages geometrical information to generate synthetic views from virtual cameras at both, training and test time, resulting in normalized object appearance with respect to distance. Our synthetically generated views facilitate the detection task as they cut down the variability in visual appearance associated to objects placed at different distances from the camera. As a consequence, the deep model is relieved from learning depth-specific representations and its complexity can be significantly reduced. In particular we show that our proposed concept of exploiting virtual cameras enables us to set new state-of-the-art results on the popular KITTI3D benchmark using just a lightweight, single-stage architecture.

1. Introduction

With the advent of autonomous driving, significant attention has been devoted in the computer vision and robotics communities to the semantic understanding of urban scenes. In particular, object detection is one of the most prominent challenges that must be addressed in order to build autonomous vehicles able to drive safely over long distances.

Object detection represents a long standing problem in computer vision [17]. In the last decade, thanks to the emergence of deep neural networks and to the availability of large-scale annotated datasets, the state of the art in 2D object detection has improved significantly [11, 15, 18, 24, 25, 26], reaching near-human performance [17]. However, detecting objects in the image plane and, in general, reasoning in 2D, is not sufficient for autonomous driving applications. Safe navigation of self-driving cars requires accurate 3D localization of vehicles, pedestrians and, in general, any object in the scene. As a consequence, depth information is needed. While depth can be obtained from expensive LiDAR sensors or stereo camera rigs, recently, there has been an increasing interest in replacing them with cheaper sensors, such as RGB cameras. Unsurprisingly, state-of-the-art 3D detection methods exploit a multi-modal approach, combining data from RGB images with LiDAR information [13, 30, 31, 34]. However, recent works have attempted to recover the 3D location and pose of objects from a monocular RGB input [1, 9, 32], with the ultimate goal of replacing LiDAR with cheaper sensors such as off-the-shelf cameras. Despite the ill-posed nature of the problem, these works have shown that it is possible to infer the 3D position and pose of vehicles in road scenes given a single image with a reasonable degree of accuracy.

This work advances the state of the art by introducing MoVi-3D, a novel, *single-stage* architecture for *monocular 3D object detection*, and new training and inference schemes, which exploit geometrical prior knowledge to

synthesize new views from *virtual cameras* that are then fed to our 3D object detector (see Fig.1). Our goal is to train a network that is able to generalize across depths and build representations for an object that are independent from the actual depth of the object in the scene. The intuition is that this invariance can be achieved by virtually moving a camera in front of a potential object of interest before running the detector. By doing so, we can limit the range of depths where the network is supposed to detect an object. Similarly, at inference time, virtual views are generated to compute the final predictions. An advantage of our approach is that it can sidestep the burden of learning depth-specific features that are needed to distinguish objects at different depths (and, hence, scale), thus enabling the use of simpler models. For this reason, we can tackle successfully the 3D object detection problem with a lightweight, single-stage architecture in the more challenging multi-class setting.

We evaluate our proposed *virtual cameras* in combination with our *single-stage* architecture on the KITTI 3D Object Detection benchmark [5], comparing with state-of-the-art methods, and perform an extensive ablation study to assess the validity of our architectural choices. Thanks to our novel training strategy, despite its simplicity, our method is currently the best performing monocular 3D object detection method on KITTI3D that makes no use of additional information at both training and inference time, while relying solely on the provided annotated 3D bounding boxes.

2. Related Work

We review recent works on monocular 3D object detection covering both, approaches based on RGB only and those using depth, pseudo-LiDAR or 3D shape information.

RGB data only. 3D object detection from RGB input is inherently challenging as depth information is not available. To compensate for the ill-posed nature of the problem, previous approaches have devised different strategies. Deep3DBox [20] proposes to estimate the full 3D pose and the dimensions of objects from 2D bounding boxes by considering projective geometry constraints. OFTNet [27] considers an orthographic feature transform to map image-level features into a 3D voxel map. The map is subsequently reduced to a 2D representation (birds-eye view). Mono3D [4] generates 3D candidate boxes and scores them according to semantic segmentation, contextual, shape and class-specific features. At test time boxes are computed based on RGB images only, but the method requires semantic and instance segmentation maps as input.

ROI-10D [19] proposes a deep architecture equipped with a loss that operates directly in the space of 3D bounding boxes. In [16], the authors employ a deep network to compute the fitting degree between the proposals and the object in terms of 3D IoU scores, and introduce an approach to filter the estimated box proposals based on 2D object cues

only. To avoid computing features only from 2D proposals, GS3D [12] proposes to derive a coarse cuboid and to extract features from the visible surfaces of the projected cuboid.

MonoGRNet [23] uses a deep network with four specialized modules for different tasks: 2D detection, instance depth estimation, 3D location estimation and local corner regression. The network operates by first computing the depth and 2D projection of the 3D box center and then estimating the corner coordinates locally. MonoDIS [32] describes a two-stage architecture for monocular 3D object detection which disentangles dependencies of different parameters by introducing a novel loss enabling to handle groups of parameters separately. MonoPSR [9] uses a deep network to jointly compute 3D bounding boxes from 2D ones and estimate instance point clouds in order to recover shape and scale information.

M3D-RPN [1] and SS3D [8] are the most closely-related approaches to ours. They also implement a single-stage multi-class model. In particular, the former proposes an end-to-end region proposal network using canonical and depth-aware convolutions to generate the predictions, which are then fed to a post-optimization module. SS3D [8] proposes to detect 2D key-points as well as predict object characteristics with their corresponding uncertainties. Similarly to M3D-RPN, the predictions are subsequently fed to an optimization procedure to obtain the final predictions. Both M3D-RPN and SS3D apply a post-optimization phase and, differently from our approach, these methods benefit from a multi-stage training procedure.

Including depth or pseudo-LiDAR. Some works are based on the idea that more accurate 3D detections can be obtained with the support of depth maps or pseudo-LiDAR point clouds automatically generated from image input. For instance, ROI-10D [19] exploits depth maps inferred with SuperDepth [22]. Pseudo-Lidar [33] takes advantage of pre-computed depth maps to convert RGB images to 3D point clouds. Then, state-of-the-art LiDAR-based 3D object detection methods are employed. Pseudo-Lidar++ [35] improves over the Pseudo-LiDAR framework adapting the stereo network architecture and the loss function for direct depth estimation, thus producing more accurate predictions for far away objects.

Including 3D shape information. 3D-RCNN [10] proposes a convolutional network based on inverse-graphics which maps image regions to the 3D shape and pose of an object instance. In [36] the problem of scene understanding is addressed from the perspective of 3D shape modeling, and a 3D scene representation is proposed to jointly reason about the 3D shape of multiple objects. Deep-MANTA [2] uses a multi-task deep architecture for simultaneous vehicle detection, part localization, part visibility characterization and 3D dimension estimation. Mono3D++ [7] uses a morphable wireframe model for estimating vehicles' 3D shape

and pose and optimizes a projection consistency loss between the generated 3D hypotheses and the corresponding 2D pseudo-measurements. In [21] a shape-aware scheme is proposed in order to estimate the 3D pose and shape of a vehicle, given the shape priors encoded in form of keypoints.

3. Problem Description

In this work we address the problem of monocular 3D object detection. Given a single RGB image, the task consists in predicting 3D bounding boxes and an associated class label for each visible object. The set of object categories is predefined and we denote by n_c the total number of categories. In contrast to many other methods in the literature, our method makes no use of additional information such as pairs of stereo images, or depth derived from LiDAR or obtained from monocular depth predictors (supervised or self-supervised). In order to boost their performance, the latter approaches tend to use depth predictors that are pre-trained on the same dataset where monocular 3D object detection is going to be run. Accordingly, the setting we consider is the hardest and in general ill-posed. The only training data we rely on consists of RGB images with corresponding annotated 3D bounding boxes. Nonetheless, we assume that per-image camera calibrations are available at both training and test time.

4. Virtual Cameras

A deep neural network that is trained to detect 3D objects in a scene from a single RGB image is forced to build multiple representations for the same object, in a given pose, depending on the distance of the object from the camera. This is, on the one hand, inherently due to the scale difference that two objects positioned at different depths in the scene exhibit when projected on the image plane. On the other hand, it is the scale difference that enables the network to regress the object’s depth. In other words, the network has to build distinct representations devoted to recognize objects at specific depths and there is little margin of generalization across different depths. As an example, if we train a 3D car detector by limiting examples in a range of maximum 20m and then at test time try to detect objects at distances larger than 20m, the detector will fail to deliver proper answers. This happens because it lacks the ability to generalize across depths. As a consequence, when we train the 3D object detector we need to scale up the network’s capacity as a function of the depth ranges we want to be able to cover and scale up accordingly the amount of training data, in order to provide enough examples of objects positioned at several possible depths.

Our goal is to devise a training and inference procedure that allows the network to actually generalize across depths and build representations for an object that are independent

from the actual depth of the object in the scene. The intuition behind our work is that this invariance can be achieved by virtually moving a camera in front of each object and detect the object from that view. By doing so, indeed, objects will appear the same independently from their depth with respect to the original camera, thus enabling generalization across depth. However, we have a chicken-egg problem, because we need to know the location of the 3D objects in advance in order to move the camera there. In the following, we will show that this problem is actually easy to circumvent by properly designing the training and inference stages.

Virtual camera. We create a virtual camera by specifying a desired view window in 3D space, parallel to the camera image plane and positioned at some depth Z_v . The top-left corner of the window in 3D space, with the Y -axis pointing downwards, is given by (X_v, Y_v, Z_v) and the window has a pre-defined height H_v thus spanning the range $[Y_v - H_v, Y_v]$ along the Y -axis (see Fig. 2). We also specify a desired resolution $h_v \times w_v$ for the images that should be generated from the virtual camera. Let $x_v = \frac{X_v}{Z_v} f_x + c_x$ and $y_v = \frac{Y_v}{Z_v} f_y + c_y$ be the projection of (X_v, Y_v, Z_v) onto the real camera image plane, where $f_{x/y}$ are the x/y focal lengths and $c_{x/y}$ are the center parameters. Then, the intrinsic matrix K_{virt} that allows to map 3D points in the real camera reference system to the image plane of the virtual camera is given by

$$K_{\text{virt}} = \begin{bmatrix} s_x Z_v & 0 & -s_x X_v \\ 0 & s_y Z_v & -s_y Y_v \\ 0 & 0 & 1 \end{bmatrix},$$

where the scaling factors are given by $s_y = \frac{h_v}{H_v}$ and $s_x = \frac{s_y f_x}{f_y}$. We can also determine the size W_v of the window along the X -axis using the formula $W_v = \frac{w_v}{s_x}$. Given an image captured with the real camera and a virtual camera identified by the view window described above, we can generate an image for the virtual camera (we call it *virtual image*) as follows. We compute the top-left and bottom-right corners of the window, namely (X_v, Y_v, Z_v) and $(X_v + W_v, Y_v - H_v, Z_v)$ respectively, and project them to the image plane of the real camera, yielding the top-left and bottom-right corners of the rectangle enclosing the virtual camera image. We crop it and rescale it to the desired resolution $w_v \times h_v$ to get the final output.

Training. The goal of the training procedure is to build a network that is able to make correct predictions within

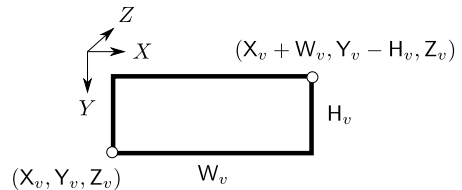


Figure 2: Notations about the virtual camera.

a limited depth range given an image from a virtual camera. Accordingly, we define a depth resolution parameter Z_{res} that is used to delimit the range of action of the network. Given a training image from the real camera and a set of ground-truth 3D bounding boxes, we generate n_v virtual images from random virtual cameras. The sampling process however is not uniform, because objects occupy a limited portion of the image and drawing virtual cameras blindly in 3D space would make the training procedure very inefficient. Instead, we opt for a ground-truth-guided sampling procedure, where we repeatedly draw (without replacement) a ground-truth object and then sample a virtual camera in a neighborhood thereof in such a way that the object is completely visible in the virtual image. In Fig. 1 we provide a real example of such a sampling result. The perturbation of the virtual camera location with respect to the position of the target ground-truth object is important in order to obtain a model that is robust to depth ranges up to the predefined depth resolution Z_{res} , which in turn plays an important role at inference time. Specifically, we position the virtual camera in a way that $Y_v = \hat{Y}$ and $Z_v = \hat{Z}$, where \hat{Y} and \hat{Z} are the upper and lower bounds of the target ground-truth box along the Y - and Z -axis, respectively. From there, we shift Z_v by a random value in the range $[-\frac{Z_{\text{res}}}{2}, 0]$, perturb randomly X_v in a way that the object is still entirely visible in the virtual image and perturb Y_v within some pre-defined range. The ground-truth boxes with \hat{Z} falling outside the range of validity $[0, Z_{\text{res}}]$ are set to *ignore*, *i.e.* there will be no training signal deriving from those boxes but at the same time we will not penalize potential predictions intersecting with this area. Our goal is to let the network focus exclusively on objects within the depth resolution range, because objects out of this range will be captured by moving the virtual camera as we will discuss below when we illustrate the inference strategy. Every other ground-truth box that is still valid will be shifted along the Z -axis by $-Z_v$, because we want the network to predict a depth value that is relative to the virtual camera position. This is a key element to ensure invariance across depth. In addition, we let a small share of the n_v virtual images to be generated by virtual cameras randomly positioned in a way that the corresponding virtual image is completely contained in the original image. Finally, we have also experimented a class-uniform sampling strategy that ensures that we have an even number of virtual images for each class that is present in the original image.

Inference. At inference time we would ideally put the virtual camera in front of potential objects in order to have the best view for the detector. Clearly, we do not know in advance where the objects are, but we can exploit the special training procedure that we have used to build the model and perform a complete sweep over the input image by taking depth steps of $\frac{Z_{\text{res}}}{2}$ and considering objects lying close

to the ground, *i.e.* we set $Y_v = 0$. Since we have trained the network to be able to predict at distances that are twice the depth step, we are reasonably confident that we are not missing objects, in the sense that there will be at least a virtual camera that captures each object. Also, due to the convolutional nature of the architecture we adjust the width of the virtual image in a way to cover the entire extent of the input image. By doing so we have virtual images that become wider as we increase the depth, following the rule $w_v = s_y \frac{Z_v}{f_y} W$, where W is the width of the input image. We finally perform NMS over detections that have been detected in the same virtual image.



Figure 3: Example of virtual images generated for inference. We show the first 10 virtual images extracted starting from depth 4.5, every 2.5m (bottom-up).

5. Proposed Single-Stage Architecture

We propose a *single-stage*, fully-convolutional architecture for 3D object detection (*MoVi-3D*), consisting of a small backbone to extract features and a simple 3D detection head providing dense predictions of 3D bounding boxes. Details about its components are given below.

5.1. Backbone

The backbone we adopt is a ResNet34 [6] with a Feature Pyramid Network (FPN) [14] module on top. The structure of the FPN network differs from the original paper [15] for we implement only 2 scales, connected to the output of modules conv4 and conv5 of ResNet34, corresponding to downsampling factors of $\times 16$ and $\times 32$, respectively. Moreover, our implementation of ResNet34 differs from the original one by replacing BatchNorm+ReLU layers with synchronized InPlaceABN (iABN^{sync}) activated with LeakyReLU with negative slope 0.01 as proposed in [28]. This change allows to free up a significant amount of GPU memory, which can be exploited to scale up the batch size and, therefore, improve the quality of the computed gradients. In Fig. 4 we depict our backbone, where white rectangles in the FPN module denote 1×1 or 3×3

convolution layers with 256 output channels, each followed by iABN^{sync}.

Inputs. The backbone takes in input an RGB image x .

Outputs. The backbone provides 2 output tensors, namely $\{f_1, f_2\}$, corresponding to the 2 different scales of the FPN network with downsampling factors of $\times 16$ and $\times 32$, each with 256 feature channels (see, Fig. 4).

5.2. 3D Detection Head

We build the 3D detection head by modifying the single-stage 2D detector implemented in RetinaNet [15]. We apply the detection module independently to each output f_i of our backbone, thus operating at a different scale of the FPN as described above. The detection modules that we apply at the different outputs of the backbone share the same parameters and provide dense 3D bounding boxes predictions. In addition, we let the module regress 2D bounding boxes similar to [1, 32], but in contrast to those works, we will not use the predicted 2D bounding boxes but rather consider this as a regularizing side task. Akin to RetinaNet, this module makes use of so-called *anchors*, which implicitly provide some pre-defined 2D bounding boxes that the network can modify. The number of anchors per spatial location is given by n_a . Fig. 4 shows the architecture of our 3D detection head. It consists of two parallel branches, the top one devoted to provide confidences about the predicted 2D and 3D bounding boxes, while the bottom one is devoted to regressing the actual bounding boxes. White rectangles denote 3×3 convolutions with 128 output channels followed by iABN^{sync}. More details about the input and outputs of this module are given below, by following the notation adopted in [32].

Inputs. The 3D detection head takes $f_i, i \in \{1, 2\}$, i.e. an output tensor of our backbone, as input. Each tensor f_i has a spatial resolution of $w_i \times h_i$.

Outputs. The detection head outputs a 2D bounding box and n_c 3D bounding boxes (with confidences) for each anchor a and spatial cell g of the $w_i \times h_i$ grid of f_i . Each anchor a provides a reference size (w_a, h_a) for the 2D bounding box. The 2D bounding box is given in terms of $\theta_{2D} = (\delta_u, \delta_v, \delta_w, \delta_h)$ and $\zeta_{2D} = (\zeta_{2D}^1, \dots, \zeta_{2D}^{n_c})$ from which we can derive

- $p_{2D}^c = (1 + e^{-\zeta_{2D}^c})^{-1}$, i.e. the probability that the 2D bounding box belongs to class c ,
- $(u_b, v_b) = (u_g + \delta_u w_a, v_g + \delta_v h_a)$, i.e. the bounding box's center, where (u_g, v_g) are the image coordinates of cell g , and
- $(w_b, h_b) = (w_a e^{\delta_w}, h_a e^{\delta_h})$, i.e. the size of the bounding box.

In addition to the 2D bounding box, the head returns for each class $1 \leq c \leq n_c$ a 3D bounding box in terms of $\theta_{3D} = (\Delta_u, \Delta_v, \Delta_z, \delta_W, \delta_H, \delta_D, r_x, r_z)$ and ζ_{3D} (we omit-

ted the superscript c). Indeed, from those outputs we can compute

- $p_{3D|2D}^c = (1 + e^{-\zeta_{3D}})^{-1}$, i.e. the confidence about the 3D bounding box being correct for class c ,
- $c = (u_b + \Delta_u, v_b + \Delta_v)$, i.e. the 3D bounding box center projected on the image plane,
- $z = \mu_z^c + \sigma_z^c \delta_z$, i.e. the depth of the bounding box center, where μ_z^c and σ_z^c are class- and Z_{res} -specific depth mean and standard deviation,
- $s = (W_0^c e^{\delta_W}, H_0^c e^{\delta_H}, D_0^c e^{\delta_D})$, i.e. the 3D bounding box dimensions, where (W_0^c, H_0^c, D_0^c) is a reference size for 3D bounding boxes belonging to class c , and
- $\alpha = \text{atan2}(r_x, r_z)$ is the rotation angle on the XZ -plane with respect to an allocentric coordinate system.

The actual confidence of each 3D bounding box is computed by combining the 2D and 3D bounding box probabilities into $p_{3D}^c = p_{3D|2D}^c p_{2D}^c$.

Losses. The losses we employ to regress the 2D bounding boxes and to learn the 2D class-wise confidence are inherited from the RetinaNet 2D detector [15]. Also the logic for the assignment of ground-truth boxes to anchors is taken from the same work, but we use it in a slightly different way, since we have 3D bounding boxes as ground-truth. The idea is to extract the 2D bounding box from the projected 3D bounding box and use this to guide the assignment of the ground-truth box to anchors. As for the losses pertaining to the 3D detection part, we exploit the lifting transformation combined with the loss disentangling strategy as proposed in [32]. Indeed, the lifting transformation allows to sidestep the issue of finding a proper way of balancing losses for the different outputs of the network, which inherently operate at different scales, by optimizing a single loss directly at the 3D bounding box level. However, this loss entangles the network's outputs in a way that renders the training dynamics unstable, thus harming the learning process. Nonetheless, the latter issue can be overcome by employing the disentangling transformation proposed in [32]. We refer to the latter work for further details.

6. Experiments

In this section we validate our contributions on the KITTI3D dataset [5]. After an initial description of the dataset, we provide details about the implementation of our method. Then, we show the results obtained comparing our single-stage architecture *MoVi-3D* against state-of-the-art methods on the KITTI3D benchmark. Finally, to better highlight the importance of our novel *virtual cameras* view definition, we perform an in-depth ablation study.

6.1. Datasets and Experimental Protocol

About the dataset. The KITTI3D dataset is arguably the most influential benchmark for monocular 3D object detec-

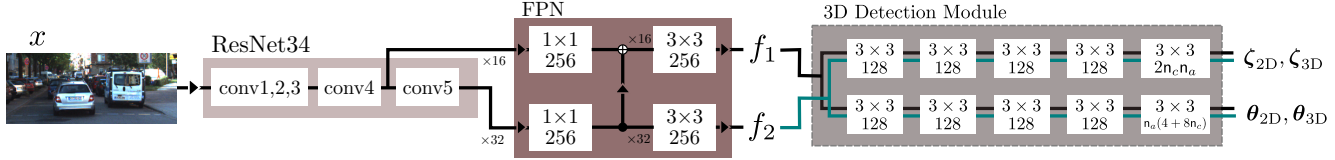


Figure 4: Our architecture. The backbone consists of a ResNet34 with a reduced FPN module covering only 2 scales at $\times 16$ and $\times 32$ downsampling factors. The 3D detection head is run independently on f_1 and f_2 . Rectangles in FPN and the 3D detection head denote convolutions followed by iABN^{sync}. See Sec. 5.2 for a description of the different outputs.

tion. It is characterized by 7481 training and 7518 test images captured in Karlsruhe, Germany, during 2011. Since the dataset does not provide an official validation set, it is common practice to split the training data into 3712 training and 3769 validation images as proposed in [3] and then report validation results. For this reason it is also mandatory not to limit the analysis of the results to the validation set, which could be biased due to snapshot cherry-picking, but instead to provide results on the official test set obtained via the KITTI3D benchmark evaluation server. The dataset annotations are provided in terms of 3D bounding boxes, each one characterized by a *category* and a *difficulty*. While the dataset includes annotations for eight different classes, the evaluation is carried out only on the three most represented ones namely *Car*, *Pedestrian* and *Cyclist*. Each box is also assigned to a *difficulty* class, *i.e.* *easy*, *moderate* and *hard*. The difficulty is determined by the distance of the object from the reference vehicle, the degree of occlusion and the level of truncation.

Experimental Protocol. In order to fairly compare with previous methods we follow the experimental protocol in [1, 8] and show results on all the KITTI3D classes obtained by means of a *single multi-class* model. We would like to remark that to our knowledge the only multi-class, monocular, RGB-only methods available in the literature are M3D-RPN [1] and SS3D [8]. For the sake of completeness we also report results associated to other methods. However, these results correspond to a different experimental protocol where training and evaluation are performed on each class independently. As specified by the Official KITTI3D evaluation protocol we present our results using the 3D Average Precision (AP) metric as well as the Bird’s Eye View (BEV) AP metric. The AP is a well-established metric [29] which assesses the quality of a method by measuring the area under the interpolated Precision-Recall (PR) curve. The interpolation is performed on a precise set of recall values, which reflects the quality of the approximation. Due to a recent update of the Official KITTI3D metric computation¹, we provide our results by using the $AP|_{R_{40}}$ metric which implies the use of 40 recall values in the range of $[1/40, 2/40, \dots, 1]$ as introduced in [32]. We evaluate

our method by utilizing the official class-specific thresholds which are set, for both 3D AP and Birds-Eye-View (BEV) AP, at 0.7 for *Car* and 0.5 for *Pedestrian* and *Cyclist*.

6.2. Implementation details

In this section we provide details about our implementation and about the choice of model hyperparameters.

Dataset Pre-processing. We pre-processed the KITTI3D annotations included into the training split defined in [3] by applying the procedure described in MonoDIS [32]. This pre-processing is needed to take into account unreliable annotations, such as those associated to fully occluded objects.

Virtual Cameras. We instantiate *virtual cameras* with a parametrization that provides good performances without compromising the overall computational complexity and speed of the method. During training we generate a total of $n_v = 8$ virtual images per training image, by using a class-uniform, ground-truth-oriented sampling strategy with a probability $p_v = 0.7$, random otherwise (see Sec. 4). We set the depth resolution Z_{res} to 5m. During inference we limit the search space along depth to [4.5m, 45m]. We set the dimensions of all the generated *virtual camera* views to have height $h_v = 100$ pixels and width $w_v = 331$ pixels. We set the depth statistics as $\mu_z = 3m$ and $\sigma_z = 1m$.

3D Detection Head. We adopt 18 anchors with six aspect ratios $\{ \frac{1}{3}, \frac{1}{2}, \frac{3}{4}, 1, 2, 3 \}$ and three different scales $\{ 2s_i 2^{\frac{j}{3}} : j \in 0, 1, 2 \}$, where s_i is the down-sampling factor of the FPN level f_i . Each anchor is considered positive if its IoU with a ground truth object is greater than 0.5. To account for the presence of objects of different categories and therefore of fairly different 3D extent, we create class-wise *reference anchors*. Each *reference anchor* has been obtained by observing the dataset statistics of the training set. We define the reference *Car* size as $W_0 = 1.63m$, $H_0 = 1.53m$, $D_0 = 3.84m$, the *Pedestrian* reference as $W_0 = 0.63m$, $H_0 = 1.77m$, $D_0 = 0.83m$ and the *Cyclist* reference as $W_0 = 0.57m$, $H_0 = 1.73m$, $D_0 = 1.78m$.

Losses. We use a weight of 1 for the 2D confidence loss and for the 3D regression loss, while we set at 0.5 the weight of the 2D regression and 3D confidence loss. The Huber parameter is set to $\delta_H = 3.0$ and the 3D confidence temperature to $T = 1$ as done in [32].

Optimization. Our network is optimized in an end-to-end

¹Official KITTI3D object detection benchmark http://www.cvlibs.net/datasets/kitti/eval_object.php?obj_benchmark=3d.

Method	# classes	Training data	3D detection			Bird's eye view		
			Easy	Moderate	Hard	Easy	Moderate	Hard
OFTNet [27]	single	RGB	1.61	1.32	1.00	7.16	5.69	4.61
SS3D [8]	multi	RGB	2.31	1.78	1.48	16.33	11.52	9.93
FQNet [16]	single	RGB	2.77	1.51	1.01	5.40	3.23	2.46
ROI-10D [19]	single	RGB+Depth	4.32	2.02	1.46	9.78	4.91	3.74
GS3D [12]	single	RGB	4.47	2.90	2.47	8.41	6.08	4.94
MonoGRNet [23]	single	RGB	9.61	5.74	4.25	18.19	11.17	8.73
MonoDIS [32]	single	RGB	10.37	7.94	6.40	17.23	13.19	11.12
MonoPSR [9]	single	RGB+LiDAR	10.76	7.25	5.85	18.33	12.58	9.91
M3D-RPN [1]	multi	RGB	14.76	9.71	7.42	21.02	13.67	10.23
Ours	multi	RGB	15.19	10.90	9.26	22.76	17.03	14.85

Table 1: Test set SOTA results on class *Car* on KITTI3D (0.7 IoU threshold)

Method	# classes	Training data	Pedestrian						Cyclist					
			3D Detection			Bird's eye view			3D Detection			Bird's eye view		
Easy	Moderate	Hard	Easy	Moderate	Hard	Easy	Moderate	Hard	Easy	Moderate	Hard	Easy	Moderate	Hard
OFTNet [27]	single	RGB	0.63	0.36	0.35	1.28	0.81	0.51	0.14	0.06	0.07	0.36	0.16	0.15
SS3D [8]	multi	RGB	2.31	1.78	1.48	2.48	2.09	1.61	2.80	1.45	1.35	3.45	1.89	1.44
M3D-RPN [1]	multi	RGB	4.92	3.48	2.94	5.65	4.05	3.29	0.94	0.65	0.47	1.25	0.81	0.78
MonoPSR [9]	single	RGB+LiDAR	6.12	4.00	3.30	7.24	4.56	4.11	8.37	4.74	3.68	9.87	5.78	4.57
Ours	multi	RGB	8.99	5.44	4.57	10.08	6.29	5.37	1.08	0.63	0.70	1.45	0.91	0.93

Table 2: Test set SOTA results on *Pedestrian* and *Cyclist* KITTI3D classes (0.5 IoU threshold)

manner and in a *single* training phase, not requiring any multi-step or warm-up procedures. We use SGD with a learning rate set at 0.2 and a weight decay of 0.0001 to all parameters but scale and biases of iABN. Following [32], we did not optimize the parameters in conv1 and conv2 of the ResNet34. Due to the fairly reduced resolution of the *virtual camera* views, we are able to train with a batch size of 2048 on 4 NVIDIA V-100 GPUs for 20k iterations, decreasing the learning rate by a factor of 0.1 at 16k and 18k iterations. No form of augmentation (*e.g.* voting using multi-scale, horizontal flipping, *etc.*) has been applied during inference.

6.3. 3D Detection

In this section we show the results of our proposed *MoVi-3D* method, providing a comparison with state-of-the-art 3D object detection methods. As previously introduced in Sec. 6.1, we would like to remind that some of the reported methods do not adopt the same experimental protocol of ours. On top of this, due to the recent redefinition of the metric computation (Sec. 6.1) the performances reported by some previous methods on the *validation* split of KITTI3D cannot be taken into consideration. For this reason we will focus our attention on the performances on the *test* split, where results can be directly derived from the Official 3D detection webpage¹.

Performances on class Car. In Tab. 1 we show the results obtained on class *Car* of the KITTI3D test set. It is evident that our approach outperforms all baselines on both 3D and BEV metrics, often by a large margin. In particular, our method achieves better performances compared to *single class* models (*e.g.* MonoDIS [32], Mono-

GRNet [23]) and to methods which use LiDAR information during training (MonoPSR [9]). Our method also outperforms the other *single-stage, multi-class* competitors (M3D-RPN [1], SS3D [8]). This is especially remarkable considering the fact that M3D-RPN relies on a fairly deeper backbone (DenseNet-121) and, similarly to SS3D, it also uses a post-optimization process. It is also worth noting that our method achieves the largest improvements on *Moderate* and *Hard* sets: on the 3D AP metric we improve with respect to the best competing method by **+12.3%** and **+24.8%** respectively while for the BEV AP metric improves by **+24.6%** and **+33.5%**, respectively.

Performances on the other KITTI3D classes. In Tab. 2 we report the performances obtained on the classes *Pedestrian* and *Cyclist* on the KITTI3D test set. On the class *Pedestrian* our approach outperforms all the competing methods on all levels of difficulty considering both 3D AP and BEV AP. Remarkably, we also achieve better performance than MonoPSR [9] which exploits LiDAR at training time, in addition to RGB images. The proposed method also outperforms the *multi-class* models in [1, 8]. On *Cyclist* our method achieves modest improvements with respect to M3D-RPN [1], but it does not achieve better performances than SS3D [8] and MonoPSR [9]. However, we would like to remark that MonoPSR [9] exploits an additional source of information (*i.e.* LiDAR) besides RGB images. SS3D [8] uses a better performing backbone than ResNet34, as claimed by the authors, and benefits from a post-optimization procedure and a multi-stage training.

Ablation studies. In Tab. 3 and Tab. 4 we show the results of different ablation studies. First, in the 1st and 2nd row of Tab. 3 we compare the performances obtained by a



Figure 5: Qualitative results obtained with *MoVi-3D* on KITTI3D.

Method	Z_{res}	Car						Pedestrian						Cyclist					
		3D Detection			Bird's eye view			3D Detection			Bird's eye view			3D Detection			Bird's eye view		
		Easy	Mod.	Hard	Easy	Mod.	Hard	Easy	Mod.	Hard	Easy	Mod.	Hard	Easy	Mod.	Hard	Easy	Mod.	Hard
MonoDIS [32]	0m	11.06	7.60	6.37	18.45	12.58	10.66	3.20	2.28	1.71	4.04	3.19	2.45	1.52	0.73	0.71	1.87	1.00	0.94
MonoDIS [32]	5m	13.40	10.89	9.67	21.90	17.38	15.71	4.98	3.31	2.59	6.30	4.33	3.38	2.09	1.07	1.00	2.70	1.42	1.31
<i>MoVi-3D</i>	20m	7.68	6.18	5.56	13.35	11.11	10.22	1.55	0.97	0.83	1.97	1.39	1.05	0.25	0.10	0.10	0.36	0.17	0.17
<i>MoVi-3D</i>	10m	11.58	9.54	8.54	17.98	15.16	13.98	1.82	1.27	0.94	2.38	1.78	1.34	1.08	0.51	0.51	1.84	0.97	0.89
<i>MoVi-3D</i>	5m	14.28	11.13	9.68	22.36	17.87	15.73	7.86	5.52	4.42	9.25	6.63	5.06	2.63	1.27	1.13	3.10	1.57	1.30
<i>MoVi-3D</i>	2.5m	13.17	10.77	9.80	20.44	16.93	15.57	4.99	3.64	2.96	6.17	4.71	3.73	3.78	1.93	1.65	4.70	2.40	2.08

Table 3: Validation set results on all KITTI3D classes. (0.7 IoU threshold on *Car*, 0.5 on *Pedestrian* and *Cyclist*).

Method	train range	val range	3D detection			Bird's eye view		
			Easy	Mod.	Hard	Easy	Mod.	Hard
MonoDIS [32]	far	near	0.2	0.1	0.1	0.2	0.1	0.1
<i>MoVi-3D</i>	far	near	4.0	1.9	1.7	5.5	2.7	2.4
MonoDIS [32]	near	far	0.2	0.1	0.1	0.2	0.2	0.1
<i>MoVi-3D</i>	near	far	3.3	1.4	1.7	4.2	1.9	2.3
MonoDIS [32]	near+far	middle	0.6	0.4	0.3	0.7	0.5	0.4
<i>MoVi-3D</i>	near+far	middle	19.2	10.6	8.8	22.9	12.8	10.4

Table 4: Ablation results on *Car* obtained by training and evaluating on different *distance* ranges.

two-stage 3D object detector MonoDIS [32] trained on *full-resolution* images with the same method but trained with our novel *virtual cameras* framework, respectively. With no exception, all the performances considering both 3D AP and BEV AP and for all the three KITTI3D classes improved in the *virtual cameras* setting. For this experiment all the hyperparameters are kept fixed as well as the training schedule of MonoDIS [32], with the only exception of the 2D anchors which have been redefined in order to take into account the fairly reduced range of object dimensions. For the application of the *virtual cameras*, we chose our best performing configuration. Second, in rows 3rd-6th of Tab. 3 we show the results of another ablation study in which we focus on the different possible configurations of the *virtual cameras* definition. In this regard, we show the performances of *MoVi-3D* by setting the *virtual camera* depth resolution Z_{res} to 20m (3rd row), 10m (4th), 5m (5th) and 2.5m (6th). Among the different settings, the depth resolution $Z_{\text{res}} = 5m$ outperforms the others by a clear margin. Finally, in Tab. 4 we conduct another ablation experiment in order to measure the generalization capabilities of our *virtual cameras*. We create different versions of the KITTI3D train/val splits, each one of them containing objects included into a specific *depth range*. In particular, we define a *far/near* train/val split, where the depth of the objects in the training split is in [0m, 20m] whereas the depth of the objects included into the validation split is in [20m,

50m]. We then define a *near/far* train/val split by reversing the previous splits, as well as a third train/val split regarded as *near+far/middle* where the training split includes object with depth in [0m, 10m] + [20m, 40m] while the validation is in [10m, 20m]. We compare the results on these three train/val splits with a strong baseline (MonoDIS [32]), setting the AP IoU threshold to 0.5. By analyzing the results in Tab. 4 it is clear that our method generalizes better across ranges, achieving performances which are one order of magnitude superior to the baseline.

Qualitative results. To conclude the section, we provide some qualitative results in Fig. 5, 6, 7 where show predictions of 3D bounding boxes of different classes.

7. Conclusions

We introduced new training and inference schemes for 3D object detection from single RGB images, designed with the purpose of injecting depth invariance into the model. At training time, our method generates synthetic views from so-called virtual cameras that are positioned within a small neighborhood of the objects to be detected. This yields to learn a model that is supposed to detect objects within a small depth range, independently from where the object was originally positioned in the scene. At inference time, we apply the trained model to multiple virtual views that span the entire range of depths at a resolution that relates to the depth tolerance considered at training time. Due to the gained depth invariance, we also designed a novel, lightweight, single-stage deep architecture for 3D object detection that does not make explicit use of regressed 2D bounding boxes at inference time, as opposed to many previous methods. Overall, our approach achieves state-of-the-art results on the KITTI3D benchmark. Future research will focus on devising data-driven methods to adaptively decide the positions of virtual cameras at inference time.



Figure 6: Example results of our MoVi-3D model on KITTI3D validation images.



Figure 7: Further example results of our MoVi-3D model on KITTI3D validation images.

References

[1] Garrick Brazil and Xiaoming Liu. M3d-rpn: Monocular 3d region proposal network for object detection. In *ICCV*, pages 9287–9296, 2019. [1](#), [2](#), [5](#), [6](#), [7](#)

[2] Florian Chabot, Mohamed Chaouch, Jaonary Rabarisoa, Celine Teuliere, and Thierry Chateau. Deep manta: A coarse-to-fine many-task network for joint 2d and 3d vehicle analysis from monocular image. In *CVPR*, July 2017. [2](#)

[3] Tianqi Chen, Mu Li, Yutian Li, Min Lin, Naiyan Wang, Minjie Wang, Tianjun Xiao, Bing Xu, Chiyuan Zhang, and Zheng Zhang. Mxnet: A flexible and efficient machine learning library for heterogeneous distributed systems. *CoRR*, abs/1512.01274, 2015. [6](#)

[4] Xiaozihi Chen, Kaustav Kundu, Ziyu Zhang, Huimin Ma, Sanja Fidler, and Raquel Urtasun. Monocular 3d object detection for autonomous driving. In *CVPR*, 2016. [2](#)

[5] Andreas Geiger, Philip Lenz, and Raquel Urtasun. Are we ready for autonomous driving? The kitti vision benchmark suite. In *CVPR*, 2012. [2](#), [5](#)

[6] Kaiming He, Xiangyu Zhang, Shaoqing Ren, and Jian Sun. Deep residual learning for image recognition. *CoRR*, abs/1512.03385, 2015. [4](#)

[7] Tong He and Stefano Soatto. Mono3d++: Monocular 3d vehicle detection with two-scale 3d hypotheses and task priors. *CoRR*, abs/1901.03446, 2019. [2](#)

[8] Eskil Jorgensen, Christopher Zach, and Fredrik Kahl. Monocular 3d object detection and box fitting trained end-to-end using intersection-over-union loss. In *CVPR*, 2019. [2](#), [6](#), [7](#)

[9] Jason Ku, Alex D. Pon, and Steven L. Waslander. Monocular 3d object detection leveraging accurate proposals and shape reconstruction. In *CVPR*, 2019. [1](#), [2](#), [7](#)

[10] Abhijit Kundu, Yin Li, and James M. Rehg. 3D-RCNN: Instance-level 3d object reconstruction via render-and-compare. In *(CVPR)*, June 2018. [2](#)

[11] Hei Law and Jia Deng. Cornernet: Detecting objects as paired keypoints. In *ECCV*, September 2018. [1](#)

[12] Buyu Li, Wanli Ouyang, Lu Sheng, Xingyu Zeng, and Xiaogang Wang. Gs3d: An efficient 3d object detection framework for autonomous driving. In *CVPR*, 2019. [2](#), [7](#)

[13] Ming Liang, Bin Yang, Yun Chen, Rui Hu, and Raquel Urtasun. Multi-task multi-sensor fusion for 3d object detection. In *CVPR*, 2019. [1](#)

[14] Tsung-Yi Lin, Piotr Dollár, Ross B. Girshick, Kaiming He, Bharath Hariharan, and Serge J. Belongie. Feature pyramid networks for object detection. *CoRR*, abs/1612.03144, 2016. [4](#)

[15] Tsung-Yi Lin, Priya Goyal, Ross B. Girshick, Kaiming He, and Piotr Dollár. Focal loss for dense object detection. *CoRR*, abs/1708.02002, 2017. [1](#), [4](#), [5](#)

[16] Lijie Liu, Jiwen Lu, Chunjing Xu, Qi Tian, and Jie Zhou. Deep fitting degree scoring network for monocular 3d object detection. *CoRR*, abs/1904.12681, 2019. [2](#), [7](#)

[17] Li Liu, Wanli Ouyang, Xiaogang Wang, Paul W. Fieguth, Jie Chen, Xinwang Liu, and Matti Pietikäinen. Deep learning for generic object detection: A survey. *CoRR*, abs/1809.02165, 2018. [1](#)

[18] Wei Liu, Dragomir Anguelov, Dumitru Erhan, Christian Szegedy, Scott Reed, Cheng-Yang Fu, and Alexander C. Berg. Ssd: Single shot multibox detector. In *ECCV*, 2016. [1](#)

[19] Fabian Manhardt, Wadim Kehl, and Adrien Gaidon. Roi10d: Monocular lifting of 2d detection to 6d pose and metric shape. In *CVPR*, 2019. [2](#), [7](#)

[20] Arsalan Mousavian, Dragomir Anguelov, John Flynn, and Jana Kosecka. 3d bounding box estimation using deep learning and geometry. In *CVPR*, July 2017. [2](#)

[21] Krishna J. Murthy, Sai G.V. Krishna, Falak Chhaya, and Madhava K. Krishna. Reconstructing vehicles from a single image: Shape priors for road scene understanding. In *ICRA*, 2017. [3](#)

[22] Sudeep Pillai, Rares Ambrus, and Adrien Gaidon. Superdepth: Self-supervised, super-resolved monocular depth estimation. In *ICRA*, 2019. [2](#)

[23] Zengyi Qin, Jinglu Wang, and Yan Lu. Monognet: A geometric reasoning network for 3d object localization. In *(AAAI)*, 2019. [2](#), [7](#)

[24] Joseph Redmon, Santosh Divvala, Ross Girshick, and Ali Farhadi. You only look once: Unified, real-time object detection. In *CVPR*, June 2016. [1](#)

[25] Joseph Redmon and Ali Farhadi. Yolo9000: Better, faster, stronger. In *CVPR*, 2017. [1](#)

[26] Shaoqing Ren, Kaiming He, Ross Girshick, and Jian Sun. Faster R-CNN: Towards real-time object detection with region proposal networks. In *NIPS*, 2015. [1](#)

[27] Thomas Roddick, Alex Kendall, and Roberto Cipolla. Orthographic feature transform for monocular 3d object detection. *CoRR*, abs/1811.08188, 2018. [2](#), [7](#)

[28] Samuel Rota Bulò, Lorenzo Porzi, and Peter Kontschieder. In-place activated batchnorm for memory-optimized training of DNNs. In *CVPR*, 2018. [4](#)

[29] Gerard Salton and Michael J. McGill. *Introduction to Modern Information Retrieval*. McGraw-Hill, Inc., New York, NY, USA, 1986. [6](#)

[30] Shaoshuai Shi, Xiaogang Wang, and Hongsheng Li. Pointrcnn: 3d object proposal generation and detection from point cloud. In *CVPR*, 2019. [1](#)

[31] Kiwoo Shin, Youngwook Paul Kwon, and Masayoshi Tomizuka. Roarnet: A robust 3d object detection based on region approximation refinement. *CoRR*, abs/1811.03818, 2018. [1](#)

[32] Andrea Simonelli, Samuel Rota Bulò, Lorenzo Porzi, Manuel López-Antequera, and Peter Kontschieder. Disentangling monocular 3d object detection. In *ICCV*, 2019. [1](#), [2](#), [5](#), [6](#), [7](#), [8](#)

[33] Yan Wang, Wei-Lun Chao, Divyansh Garg, Bharath Hariharan, Mark Campbell, and Kilian Weinberger. Pseudo-lidar from visual depth estimation: Bridging the gap in 3d object detection for autonomous driving. In *CVPR*, 2019. [2](#)

[34] Zhixin Wang and Kui Jia. Frustum convnet: Sliding frustums to aggregate local point-wise features for amodal 3d object detection. *CoRR*, abs/1903.01864, 2019. [1](#)

[35] Yurong You, Yan Wang, Wei-Lun Chao, Divyansh Garg, Geoff Pleiss, Bharath Hariharan, Mark Campbell, and Kilian Q. Weinberger. Pseudo-lidar++: Accurate depth for 3d object detection in autonomous driving. *CoRR*, abs/1906.06310, 2019. [2](#)

[36] Muhammad Zeeshan Zia, Michael Stark, and Konrad Schindler. Are cars just 3d boxes? Jointly estimating the 3d shape of multiple objects. In *CVPR*, 2014. [2](#)